

# Numerical simulation of the transient aerodynamic phenomena induced by passing manoeuvres

David Uystepuyst<sup>a</sup>, Siniša Krajnović<sup>a</sup>

*<sup>a</sup>Division of Fluid Dynamics, Department of Applied Mechanics, Chalmers University of Technology, SE-41296 Gothenburg, Sweden.*

---

## Abstract

Several three-dimensional Unsteady Reynolds-Averaged Navier-Stokes (URANS) simulations of the passing generic vehicles (Ahmed bodies) are presented. The relative motion of vehicles was obtained using a combination of deforming and sliding computational grids. The vehicle studied is an Ahmed body with an angle of the rear end slanted surface of  $30^\circ$ . Several different relative velocities and transversal distances between vehicles were studied. The aerodynamic influence of the passage on the overtaken vehicle was studied. The results of the simulations were found to agree well with the existing experimental data. Numerical results were used to explain effects of the overtaking manoeuvre on the main aerodynamic coefficients.

**Keywords:** Passing manoeuvres, Overtaking vehicles, Unsteady aerodynamics, Unsteady Reynolds-Averaged Navier-Stokes, Turbulence Model, Deforming mesh, Sliding mesh

---

## **1. Introduction**

The overtaking manoeuvre between two vehicles yields additional aerodynamic forces acting on both vehicles. These additional forces lead to sudden lateral displacements and rotations around the yaw axis of each vehicles. Such sudden change of the side force and of the yawing moment, complicates the steering corrections performed by the driver and can yield critical safety situations, in particular in adverse weather conditions, such as crosswinds or rain. Intensities of these forces are extrapolated when the overtaking manoeuvre involves a light car and a heavy-truck. Moreover, such a manoeuvre implies a disturbance of the aerodynamic of vehicles.

The first studies on the overtaking effects, Heffrey [1] and Howell [2], were investigated in response of the weight reduction of cars involved by the first oil crisis. Actually, after this oil crisis, car manufacturers have made substantial efforts to reduce the fuel consumption. This was achieved by improving the design of the cars, by developing efficient engine or by decreasing the vehicle weight. With the third option, vehicles became more sensitive to unsteady aerodynamic effects, such as those induced by an overtaking manoeuvre. In addition to the works of Heffrey and Howell, several experimental studies were carried out as well. These studies were focused on different aspects. Studies performed by Legouis et al [3], Telionis et al [4] or Yamamoto et al [5] were dedicated to the car-truck overtaking.

More recently, several dynamic studies in order to analyze effects of the relative velocity, the transverse passing, and the crosswind during an overtaking manoeuvre were performed by Noger et al [6, 7]. Both studies were carried out with 7/10 scaled Ahmed bodies, [8]. The two bodies of the first study were hatchback shapes (slant of  $30^\circ$ ), while the two bodies of the second one were squareback shapes. Noger and Van Grevenynghe [9] proposed a study of car-truck overtaking on one test case: one relative velocity and one lateral spacing. Gilliéron and Noger [10] analyzed the transient phenomena occurring during various phenomena such as the overtaking, the crossing or tunnel exits.

The overtaking process has also been studied using numerical modelling. Some recent two-dimensional (2D) numerical studies can be found. Clark and Filipponi [11] performed the overtaking process of two sharp edged bodies. The work aimed to provide a thorough analysis of the overtaking process. Effects of the relative velocity and the transversal spacing were studied. The authors focused on 2D overtaking as a preliminary means of investigating an appropriate simulation strategy for the complex three-dimensional (3D) flow. Corin et al [12] performed 2D numerical simulations of two rounded edges bodies. The dynamic effect of the passing manoeuvre was highlighted by comparisons with quasi-steady calculations. It was shown that crosswinds yield significant dynamic

effects. The authors of [11, 12] agreed that their 2D approaches were first steps towards 3D calculations. In particular, the Venturi effect, occurring when vehicles move closer, is strongly overestimated. 3D numerical simulations of two Ahmed bodies overtaking were performed by Gilliéron [13]. Calculations were achieved using a Reynolds Averaged Navier-Stokes numerical method with a  $k - \epsilon$  turbulence model. The effects of the transversal spacing and the crosswind were studied. However, this study was limited to a quasi-steady approach.

This paper presents a dynamic three-dimensional simulation of passing processes based on the  $\zeta - f$  turbulence model and a deforming/sliding mesh method. The aims are to accurately predict the aerodynamic forces and moment, occurring on vehicles during a passing manoeuvre, and to give thorough analysis of the passing process. The paper starts with a description in section 2.1 of the experimental set-up that is used in the present numerical study. This is followed by the numerical methodology, including the turbulence model, the numerical method and details, and the deforming/sliding mesh method, in section 2.2. Results of the simulations are presented in section 3. In section 4, a complete analysis of the effects of the passing manoeuvre is provided. Finally, the paper is summarized in section 5.

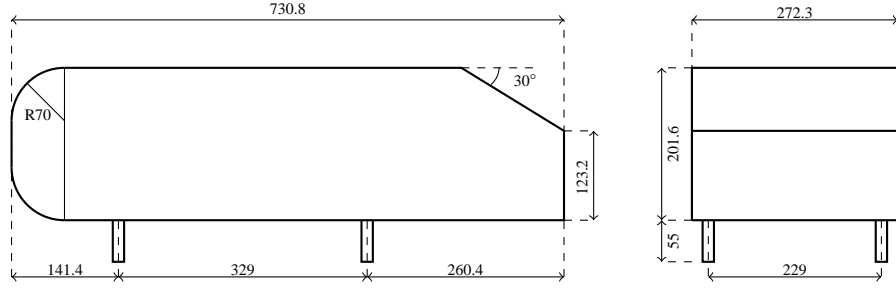


Figure 1: 7/10 scale Ahmed bluff body [8], dimensions in *mm*.

## 2. Method

### 2.1. Description of the set-up

#### 2.1.1. Geometries

The body used in this study is identical to this in the experimental work [7] and is 7/10 Ahmed bodies shown in figure 1. This body has a hatchback type rear end with an angle of  $30^\circ$ .

As it is shown, both bodies consist on rounded front end and sharpened rear end. The main vehicle sizes are: the length  $L = 730.8 \text{ mm}$ , the width  $W = 272.3 \text{ mm}$ , the height  $H = 201.6 \text{ mm}$  and the ground clearance of  $55 \text{ mm}$ . Supports are  $15 \text{ mm}$  diameter cylindrical and the length of the slant surface is  $155.4 \text{ mm}$ . The Reynolds number based on height of the vehicle is  $Re_H = 390.000$ , for a velocity of  $30 \text{ m.s}^{-1}$ .

### 2.1.2. Dimensionless coefficient

As in the experimental works of Noger et al, a dimensionless parameter  $k$  is defined as the ratio of the relative velocity  $V_r$  to a steady velocity  $V$ :

$$k = \frac{V_r}{V}. \quad (1)$$

The steady velocity is the velocity of the moving body, e.g.  $V = V_\infty + V_r$ .

During an overtaking, the strongly affected aerodynamic coefficients are the drag force coefficient  $C_d$ , the side force coefficient  $C_y$  and the yawing moment coefficient  $C_n$  given by:

$$\begin{cases} F_d = \frac{1}{2}\rho S V^2 C_d, \\ F_y = \frac{1}{2}\rho S V^2 C_y, \\ N = \frac{1}{2}\rho E S V^2 C_n, \end{cases} \quad (2)$$

where  $F_d$ ,  $F_y$  and  $N$  are respectively the drag force, the side force and the yawing moment obtained by integrating the pressure distribution around the model. In equation (2),  $\rho$  is the air density,  $S$  the body frontal area and  $E$  the longitudinal distance between the supports. Note that  $V$  is the above defined steady velocity.

### 2.1.3. Overtaking process

The figure 2 shows the sketch of the overtaking, with distances and the forces direction. The overtaking consists, as in the experimental work, on the stationary body located in the middle of the wind tunnel length and a moving body located

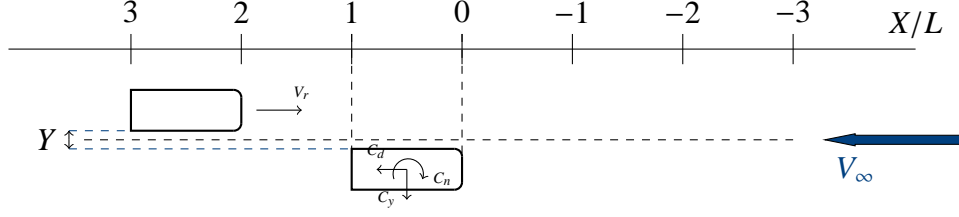


Figure 2: Notations for the vehicle positioning and aerodynamic coefficient direction.

5L behind the stationary body at the beginning of the calculation, and 5L in front of the stationary body at the end of the calculation. An inlet condition is set with the normal velocity  $V_\infty$  corresponding to the velocity of the stationary body. The moving body is set in motion with the relative velocity  $V_r$ . The reference case is set with the velocity ratio  $k$  and the transversal spacing  $Y$  at values  $k = 0.248$  ( $V_\infty = 30.32 \text{ m.s}^{-1}$  and  $V_r = 10 \text{ m.s}^{-1}$ ) and  $Y = 0.25W$ .

## 2.2. Numerical methodology

### 2.2.1. Governing equations and turbulence model

The flow around vehicles was predicted using the Reynolds-Averaged Navier Stokes equations coupled with the eddy viscosity  $\zeta - f$  model equations [14]. The continuity and momentum equations are given by:

$$\begin{cases} \frac{\partial U_i}{\partial x_i} = 0, \\ \frac{\partial U_i}{\partial t} + U_j \frac{\partial U_i}{\partial x_j} = -\frac{1}{\rho} \frac{\partial P}{\partial x_i} + \frac{1}{\rho} \frac{\partial}{\partial x_j} (\tau_{ij} - \rho \overline{u_i u_j}), \end{cases} \quad (3)$$

where  $U_i$  is the mean-velocity vector,  $\rho$  is the fluid density,  $P$  the mean-pressure,  $\tau_{ij}$  denotes the mean viscous stress tensor:

$$\tau_{ij} = 2\mu S_{ij}. \quad (4)$$

In the equation (4),  $\mu$  is the dynamic viscosity and the mean strain rate tensor  $S_{ij}$  is given by:

$$S_{ij} = \frac{1}{2} \left( \frac{\partial U_i}{\partial x_j} + \frac{\partial U_j}{\partial x_i} \right).$$

The last term of equation (3) is the unknown Reynolds stress tensor which must be modeled.

The Reynolds stress tensor is expressed with the Boussinesq's analogy:

$$-\rho \overline{u_i u_j} = 2\rho \nu_t S_{ij} - \frac{2}{3} \rho k \delta_{ij},$$

where  $\nu_t$  is the turbulent viscosity and  $\delta_{ij}$  is the Kronecker delta. In the  $\zeta - f$  model, the eddy-viscosity is defined as:

$$\nu_t = C_\mu \zeta k \tau,$$

where  $\tau$  is the time scale given as:

$$\tau = \max \left[ \min \left( \frac{k}{\varepsilon}, \frac{a}{\sqrt{6} C_\mu |S| \zeta} \right), C_\tau \left( \frac{\nu}{\varepsilon} \right)^{1/2} \right].$$

The velocity scale ratio  $\zeta$  is obtained from the following equation:

$$\frac{D\zeta}{Dt} = f - \frac{\zeta}{k} \mathcal{P}_k + \frac{\partial}{\partial x_k} \left[ \left( \nu + \frac{\nu_t}{\sigma_\zeta} \right) \frac{\partial \zeta}{\partial x_k} \right].$$

The equations of the turbulent kinetic energy and its dissipation are:

$$\begin{aligned} \frac{Dk}{Dt} &= (\mathcal{P}_k - \varepsilon) + \frac{\partial}{\partial x_j} \left[ \left( \nu + \frac{\nu_t}{\sigma_k} \right) \frac{\partial k}{\partial x_j} \right] \\ \frac{D\varepsilon}{Dt} &= \frac{C_{\varepsilon 1} \mathcal{P}_k - C_{\varepsilon 2} \varepsilon}{\tau} + \frac{\partial}{\partial x_j} \left[ \left( \nu + \frac{\nu_t}{\sigma_\varepsilon} \right) \frac{\partial \varepsilon}{\partial x_j} \right]. \end{aligned}$$



| $C_\mu$ | $C_{\varepsilon 1}$    | $C_{\varepsilon 2}$ | $c_1$ | $C'_2$ | $\sigma_k$ | $\sigma_\varepsilon$ | $\sigma_\zeta$ | $C_\tau$ | $C_L$ | $C_\eta$ |
|---------|------------------------|---------------------|-------|--------|------------|----------------------|----------------|----------|-------|----------|
| 0.22    | $1.4(1 + 0.012/\zeta)$ | 1.9                 | 0.4   | 0.65   | 1          | 1.3                  | 1.2            | 6.0      | 0.36  | 85       |

Table 1: Coefficients in the  $\zeta - f$  turbulence model

In above equations, the production is given by:

$$\mathcal{P}_k = -\overline{u_i u_j} \frac{\partial U_i}{\partial x_j}.$$

The elliptic relaxation function  $f$  is formulated by using the pressure-strain model of Speziale et al [15]:

$$L^2 \nabla^2 f - f = \frac{1}{\tau} \left( c_1 + C'_2 \frac{\mathcal{P}_k}{\epsilon} \right) \left( \zeta - \frac{2}{3} \right) - \left( \frac{C_4}{3} - C_5 \right) \frac{\mathcal{P}_k}{k}.$$

The length scale  $L$  is:

$$L = C_L \max \left[ \min \left( \frac{k^{3/2}}{\epsilon}, \frac{k^{1/2}}{\sqrt{6} C_\mu |S| \zeta} \right), C_\eta \left( \frac{\nu^3}{\epsilon} \right)^{1/4} \right].$$

Coefficients in above equations are given in table 1.

The  $\zeta - f$  model by Hanjalić et al [14], based on the  $\overline{\nu^2} - f$  model of Durbin [16], is very robust and more accurate than the simple two-equation eddy viscosity models.

### 2.2.2. Numerical method

The system of equations (3) was solved using a commercial solver, AVL FIRE. This software is based on a cell-centered finite volume method. The momentum equations were discretized using a second-order upwind scheme. An implicit

second-order scheme was used for the temporal discretization. The SIMPLE algorithm was used to couple the velocity and pressure fields. A collocated grid arrangement was employed.

The numerical domain is shown in figure 3. The experimental wind tunnel section is  $5\text{ m} \times 3\text{ m}$ . This section was reduced in the present simulations. The width, and the height, of the numerical domain represent respectively more than 15 times, and 7.5 times, the height of the vehicle. The length is set to  $18\text{ m}$  for the good progress of the deforming/sliding mesh strategy.

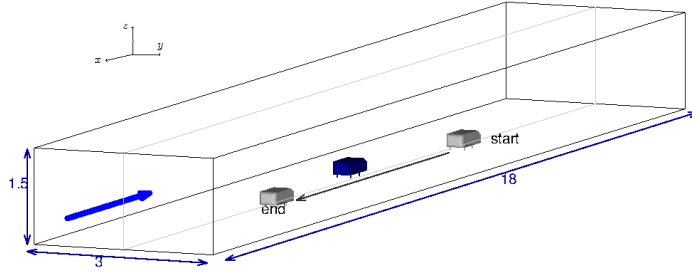


Figure 3: Computational domain (dimensions in m).

The uniform free stream velocity  $V_\infty$  was set at the inlet boundary, in front of vehicles. A static pressure was applied at the outlet. No-slip wall boundary conditions were used on the bodies and on the floor. Finally, slip wall boundary conditions were applied on the lateral and on the roof surfaces.

### 2.2.3. Numerical details

The structured grids were made with the commercial grid generator Ansys ICEM-CFD and consist of only hexahedral elements. The figure 4 shows a side view of volume and surface meshes, for the bluff body. A grid topology was constructed using several O-grids in order to concentrate most of the computational cells close to the surface of the vehicles.

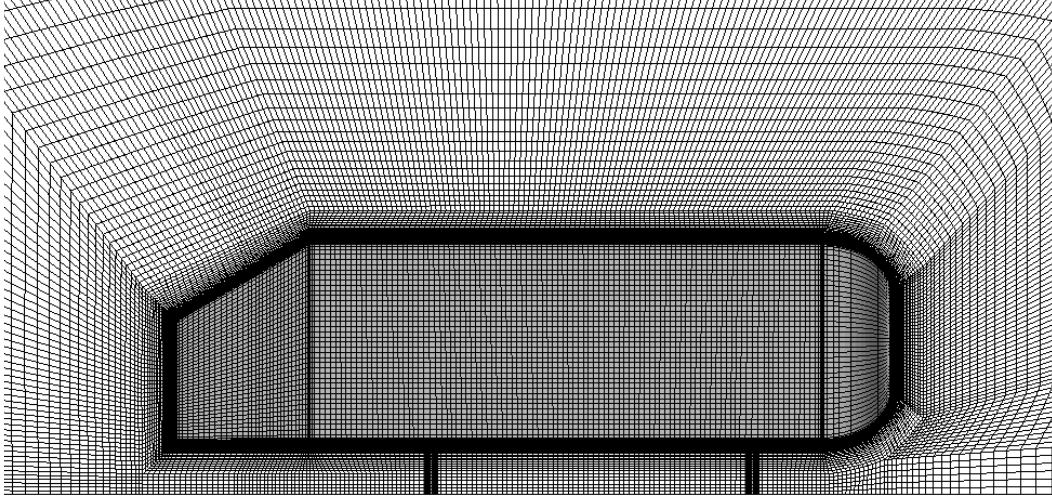


Figure 4: Surface and volume mesh of bluff body.

Accuracy was established by making the original case simulation ( $k = 0.248$  and  $Y = 0.25W$ ) on three different computational grids. The numbers of computational cells are: 4 millions for the coarse mesh, 6 millions for the middle mesh and 8 millions for the fine mesh. For a velocity of  $30 \text{ m.s}^{-1}$ , the wall normal resolution,  $n^+$ , is such that  $n^+ < 2$ ,  $n^+ < 4$  and  $n^+ < 6$  for the fine mesh, the middle

| coarse                  | middle                  | fine                    |
|-------------------------|-------------------------|-------------------------|
| $20 < \Delta s^+ < 960$ | $20 < \Delta s^+ < 580$ | $20 < \Delta s^+ < 500$ |
| $20 < \Delta l^+ < 840$ | $20 < \Delta l^+ < 560$ | $20 < \Delta l^+ < 450$ |

Table 2: Resolution in the streamwise and normal streamwise directions.

mesh and the coarse mesh, respectively. Note that the cell next to the wall should reach  $n^+$  as a maximum less than 3 with the  $\zeta-f$  model [17]. The resolution in the streamwise direction  $\Delta s^+$ , and the resolution in directions normal to streamwise  $\Delta l^+$  are reported in table 2 for the three computational meshes. The averaged  $\Delta s^+$  was 450, 350 and 300 for the coarse, the middle and the fine grid, respectively. The averaged  $\Delta l^+$  was 400, 300 and 260 for the coarse, the middle and the fine grid, respectively. Here,  $n^+ = nu_\tau/\nu$ ,  $\Delta s^+ = \Delta su_\tau/\nu$  and  $\Delta l^+ = \Delta lu_\tau/\nu$ , where  $n$  is the wall-normal distance,  $\Delta s$  is the streamwise distance,  $\Delta l$  is the spanwise distance,  $u_\tau$  is the friction velocity and  $\nu = \mu/\rho$  is the kinematic viscosity. The time step range was between  $2 \times 10^{-4}$  s and  $5 \times 10^{-4}$  s, depending on the grid and the relative velocity, giving a CFL number around 0.9 for the highest velocity and for all grids.

#### 2.2.4. Deforming and sliding mesh

The rectilinear displacement of a body was achieved by a deforming/sliding grid method. Figure 5 illustrates the effect of the body movement on the computational grid at three different times of the simulation.

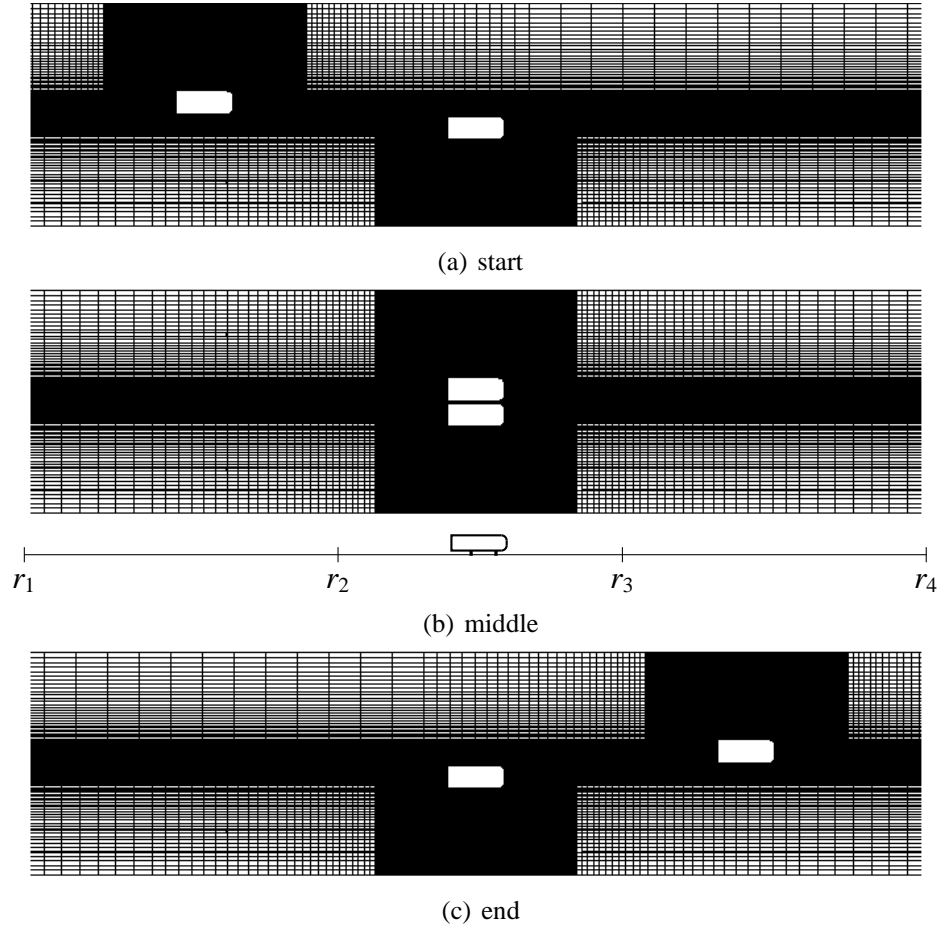


Figure 5: Deformation of the computational grid for the overtaking process.

The overall domain was composed by two subdomains: the bottom one, containing the stationary body, remained fixed all along the simulation; and the top one, containing the moving body. This last subdomain is symbolically divided in three zones  $[r_i, r_{i+1}]$ , for  $i = 1, 2, 3$ , see figure 5(b). The zone between  $r_2$  and  $r_3$  was slid during the simulation. The two remaining zones were compressed or stretched in response of the sliding movement of the central part. A similar ap-

proach was successfully used by Krajnović et al. [17, 18] for the unsteady RANS simulations of trains passing each other or exiting tunnel and for the LES simulations of a rotating vehicle. Finally a common interfacing was performed between the two meshes.

### 3. Results

#### 3.1. Numerical accuracy

Numerical accuracy was checked by comparing aerodynamic coefficients obtained on the overtaken body between calculations on different meshes. The side force and the yawing moment coefficients obtained on the three meshes, discussed in the section 2.2.3, are shown in figure 6 and compared to the experimental data.

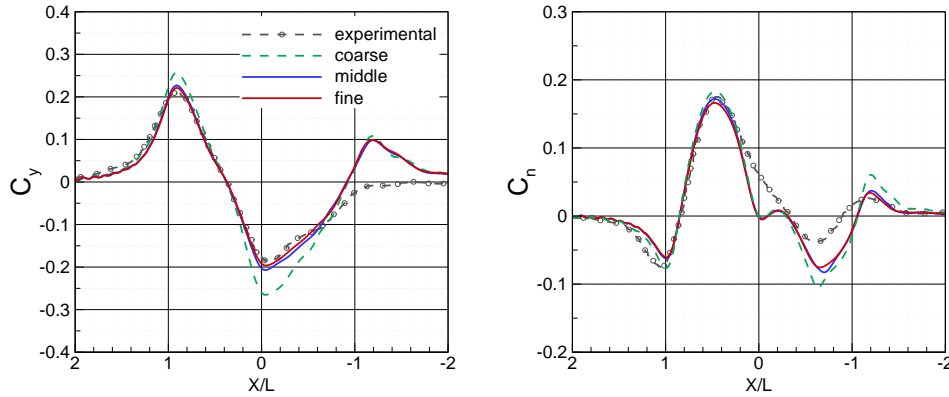


Figure 6: Mesh resolution analysis. Side force (left) and yawing moment (right) coefficients.

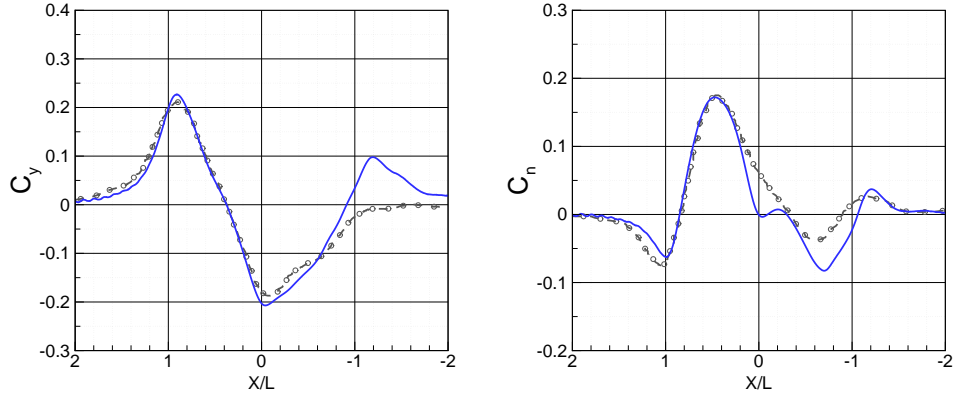
As can be seen, the coarse mesh involves a systematical overestimation of amplitudes, especially on the side force, while the middle and the fine mesh yield similar

results: relatively close to the experimental data. For the side force, the critical positions, corresponding to the minimum and the maximum value at  $X/L = 0$  and  $X/L = 1$  are in good agreement between the middle and the fine grids. For the first peak of side force, occurring at  $X/L=1$ , the maximum difference between the experimental data and the numerical results is +5% for the fine grid and +7% for the middle grid. This difference goes up to 21% for the coarse grid. For the highest peak of yawing moment, occurring at  $X/L=0.5$ , the three grids have good agreement with the experimental data with differences of +5%, +1% and -5% for the coarse, the middle and the fine grids, respectively. It is shown that the agreement between the numerical results of the middle grid and the fine grid is very good, proofing the grid convergence.

### 3.2. *Relative velocity effects*

Three cases with velocity ratios of  $k = 0.141$  ( $V_r = 5 \text{ m.s}^{-1}$ ),  $k = 0.248$  and  $k = 0.331$  ( $V_r = 15 \text{ m.s}^{-1}$ ) were simulated. Comparisons of the results obtained for the two relative velocities  $k = 0.141$  and  $k = 0.248$  are shown in figure 7 with the experimental data.

For both cases, the numerical results are in good agreement with the experimental data. Nevertheless, the overestimation of the first peak of side force by the numerical simulation is slightly larger for  $k = 0.141$  than for  $k = 0.248$ . For  $k = 0.141$ , the numerical result of side force is constant between  $X/L=0$  and  $X/L=-0.5$ , see



(a)  $k = 0.248$

(b)  $k = 0.141$

Figure 7: Relative velocity effects on the overtaken body. Side force (left) and yawing moment (right) coefficients. ( $\circ$ ) experimental, ( $\text{—}$ ) numerical.

figure 7(b). However, it is consistent with the experimental data.

Figure 8 shows comparisons of the numerical results for the three relative velocities. The drag force coefficient presented here, is subtracted from the steady drag coefficient value.



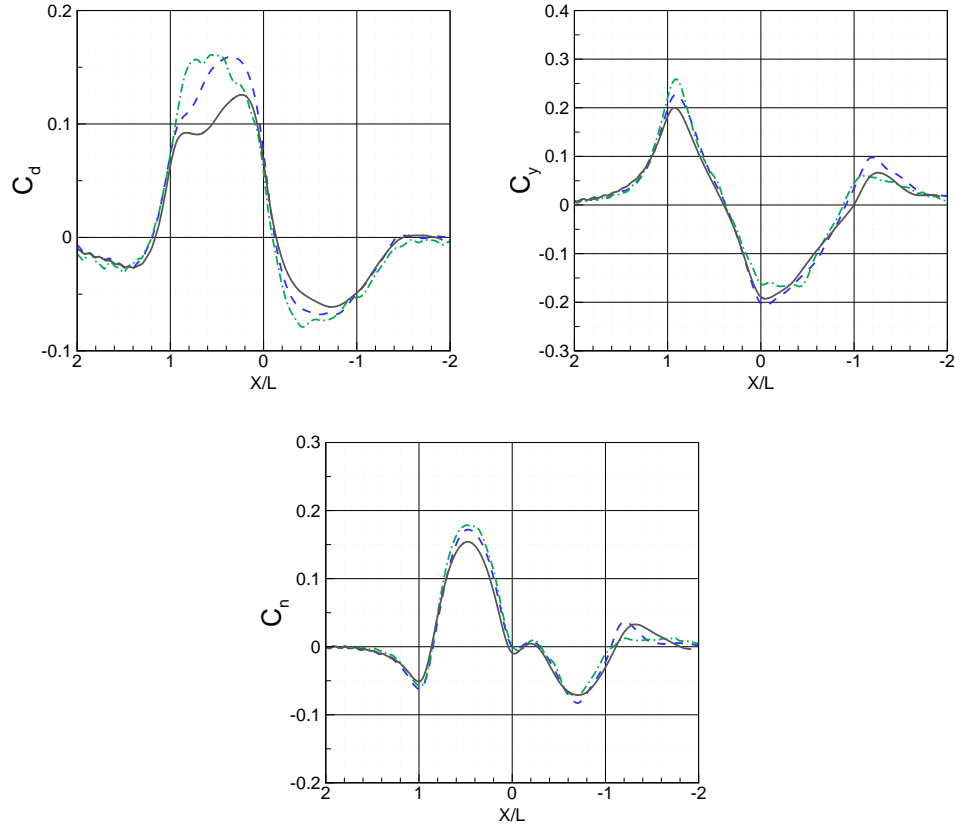


Figure 8: Relative velocity effects on the overtaken body. Drag force (top left), Side force (top right) and yawing moment (bottom) coefficients. (—)  $k = 0.331$ , (---)  $k = 0.248$ , (-.-)  $k = 0.141$ . Numerical results.

The steady drag coefficient value measured of 0.38 gave a drag increase up to 50%. This shows that the overtaking manoeuvre can yield a dramatical effect on the car aerodynamic and, therefore, on its fuel consumption.

The existing literature is divided in how the relative velocity of the vehicle influences the aerodynamic coefficients. Noger et al [6, 7] found that the aerodynamic

coefficients are independent of the relative velocity. Corin et al [12] found that when the relative velocity increased, the drag coefficient increased and the side force decreased. Clarke and Filippone [11], and Gilliéron and Noger [10], shown that an increase in relative velocity yields an increase in the peak coefficients. However, the coefficients are normalized with the velocity of the overtaken vehicle in [10, 11].

In the present study, the coefficients decrease when the relative velocity increases. When the relative velocity increases, the dynamic pressure increases. Therefore, the resulting forces occurring on the overtaken vehicle become more substantial. But these forces are normalized with the overtaking vehicle velocity which takes into account the relative velocity. This can explain the decrease of aerodynamic coefficients peaks.

### *3.3. Transverse spacing effects*

In order to study the effects of the transverse spacing, the calculation  $k = 0.248$  was carried out with two additional transverse spacings:  $Y = 0.5W$  and  $Y = 0.7W$ . To perform these new calculations, a new mesh was made to take into account the substantial difference of transversal spacing between the case  $Y = 0.25W$  and the case  $Y = 0.5W$ . This new mesh was deformed, in the transversal direction, for the calculation of the case  $Y = 0.7W$ .

The results, for the side force and the yawing moment coefficients, are shown in figure 9. For  $Y = 0.7$ , the quasi-steady numerical results obtained by Gilliéron and Noger [10] were available and were added in figure 9(b). The experimental data of the quasi-steady case are not shown here. However, these data are very close to the experimental data of the dynamic case. As said previously, the aerodynamic coefficients are independent to the relative velocity in Noger's works, indeed.

Both numerical results are in good agreement with the experimental data. Nevertheless, the numerical simulation underestimates the minimum value of the side force.

Figure 10 shows the evolution of the drag force coefficient, the side force coefficient and the yawing moment coefficient for the three different spacings:  $Y = 0.25W$ ,  $Y = 0.5W$  and  $Y = 0.7W$ . The last graph represents the evolution of the coefficient magnitudes as a function of the logarithm of the transverse spacing.

It can be easily seen that the coefficient amplitudes reduce when the transverse spacing increases. Besides, the effects occurring at  $X/L=0$  and  $X/L=-1$  are lower for the two highest spacings. The last graph shows that the evolution of magnitudes is a linear function of the logarithm of the transverse spacing. This result was already shown by Noger et al [7].

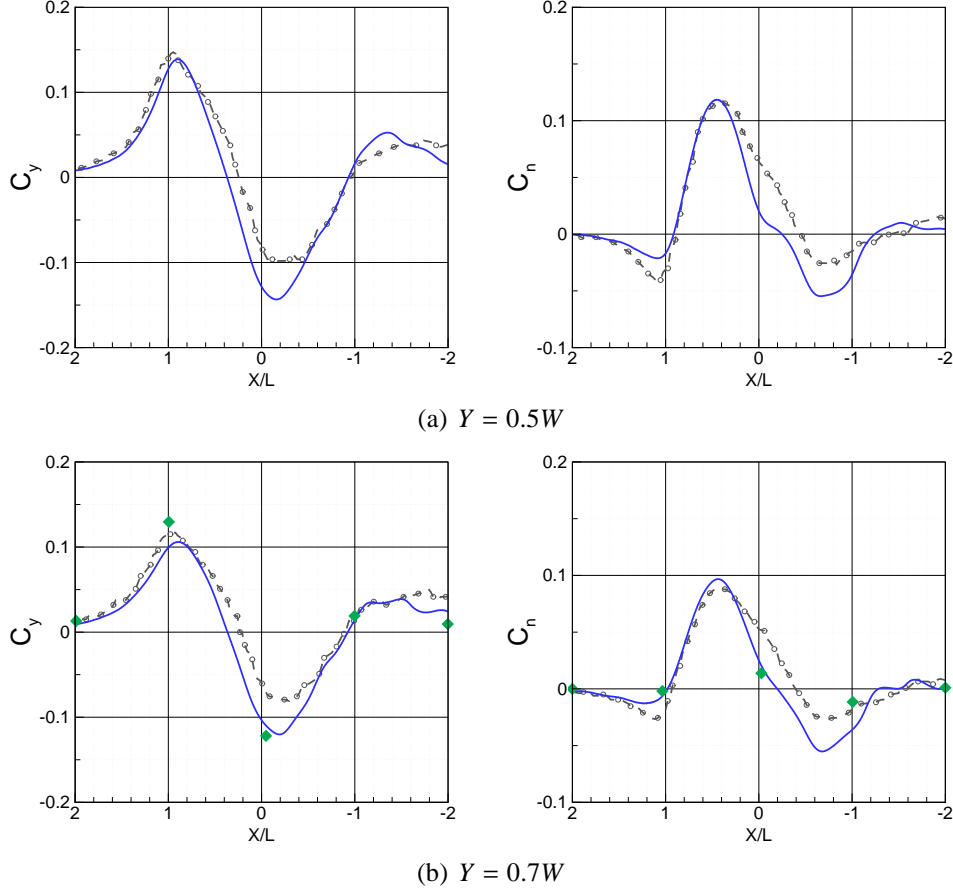


Figure 9: Transverse spacing effects on the overtaken body. Side force (left) and yawing moment (right) coefficients. ( $\ominus$ ) experimental, ( $\text{—}$ ) numerical. For  $Y = 0.7$ , ( $\blacklozenge$ ) quasi-steady numerical results of Gilliéron and Noger [10].

Figure 9(b) shows that the numerical quasi-steady approach had a tendency to overestimate the magnitude of the side force. The study of the yawing moment coefficient shows that the main phenomena were missed by the quasi-steady approach due to the bad choices of the positions studied. These two arguments prove that a dynamic approach is required for the overtaking process.

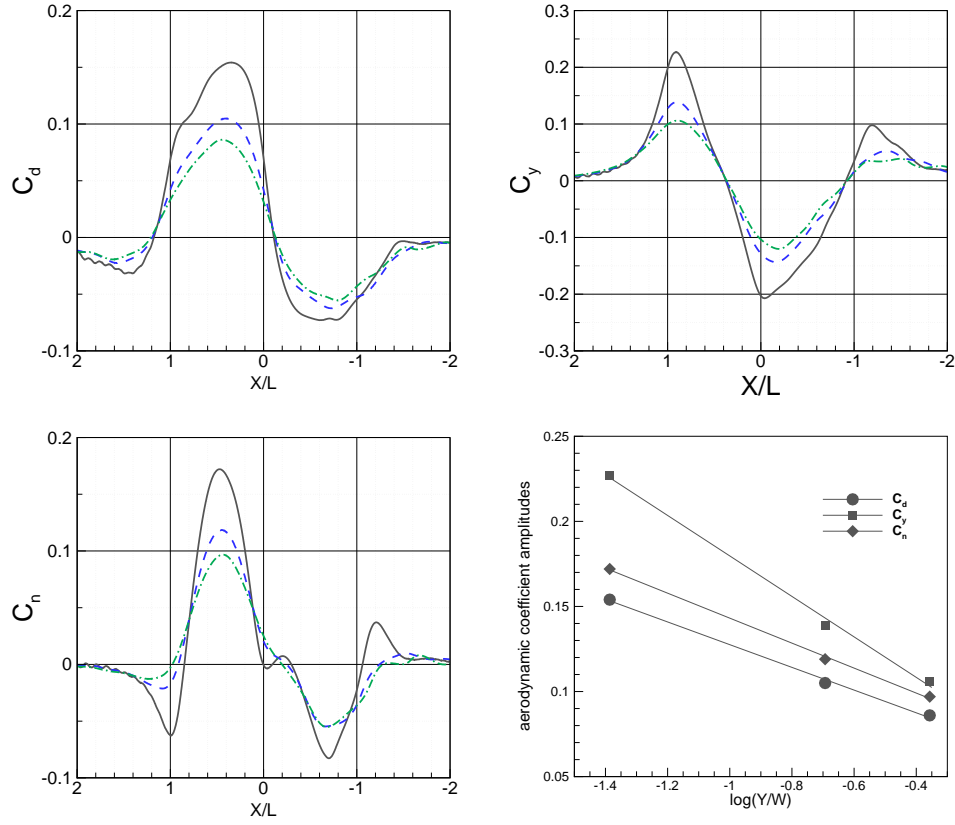


Figure 10: Transverse spacing effects on the overtaken body. Drag force coefficient (top left), side force coefficient (top right), yawing moment coefficient (bottom left) and coefficients magnitudes (bottom right). (—)  $Y = 0.25W$ , (---)  $Y = 0.5W$ , (-.-)  $Y = 0.7W$ .

## 4. Discussion of the passing manoeuvre

### 4.1. Coefficients behavior

Figure 11 shows the numerical results obtained for the drag force, the side force and the yawing moment coefficients for the reference case  $k = 0.248$  and  $Y = 0.25W$ . On these three graphs, the 5 vertical dashed lines, labelled by ⑥, ③, ④, ⑤ and ①, correspond to the critical locations for which the changes are

substantial and which require explanations. These labels were chosen to coincide with the ones of figure 12.

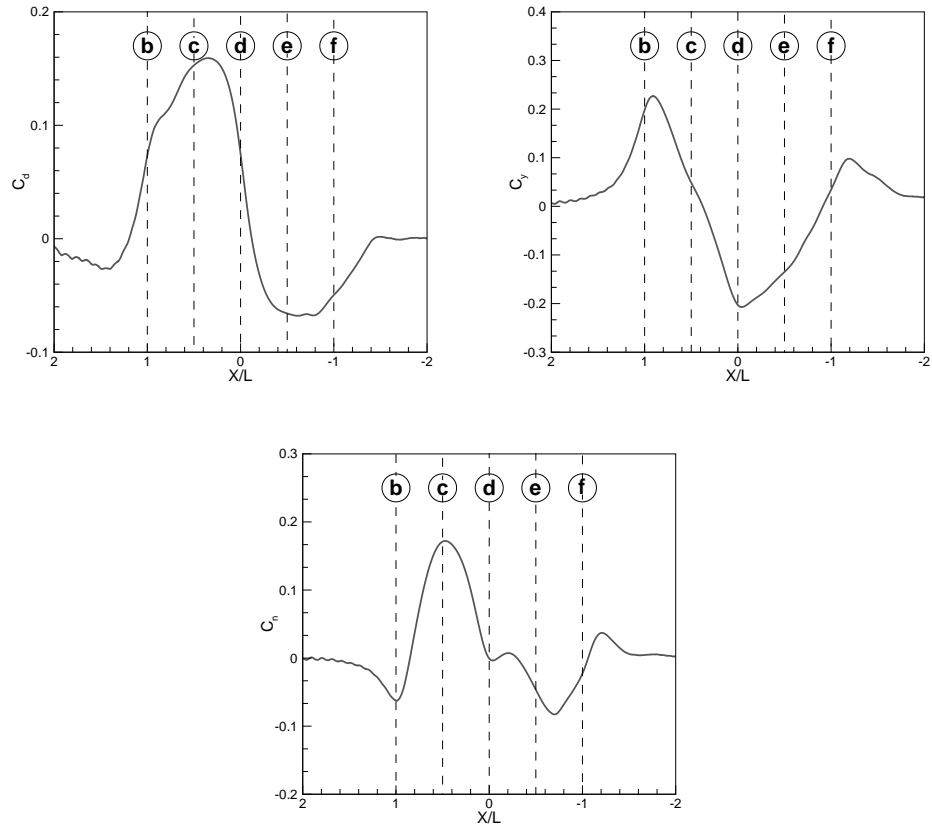


Figure 11: Drag force (top left), side force (top right) and yawing moment (bottom) coefficients.

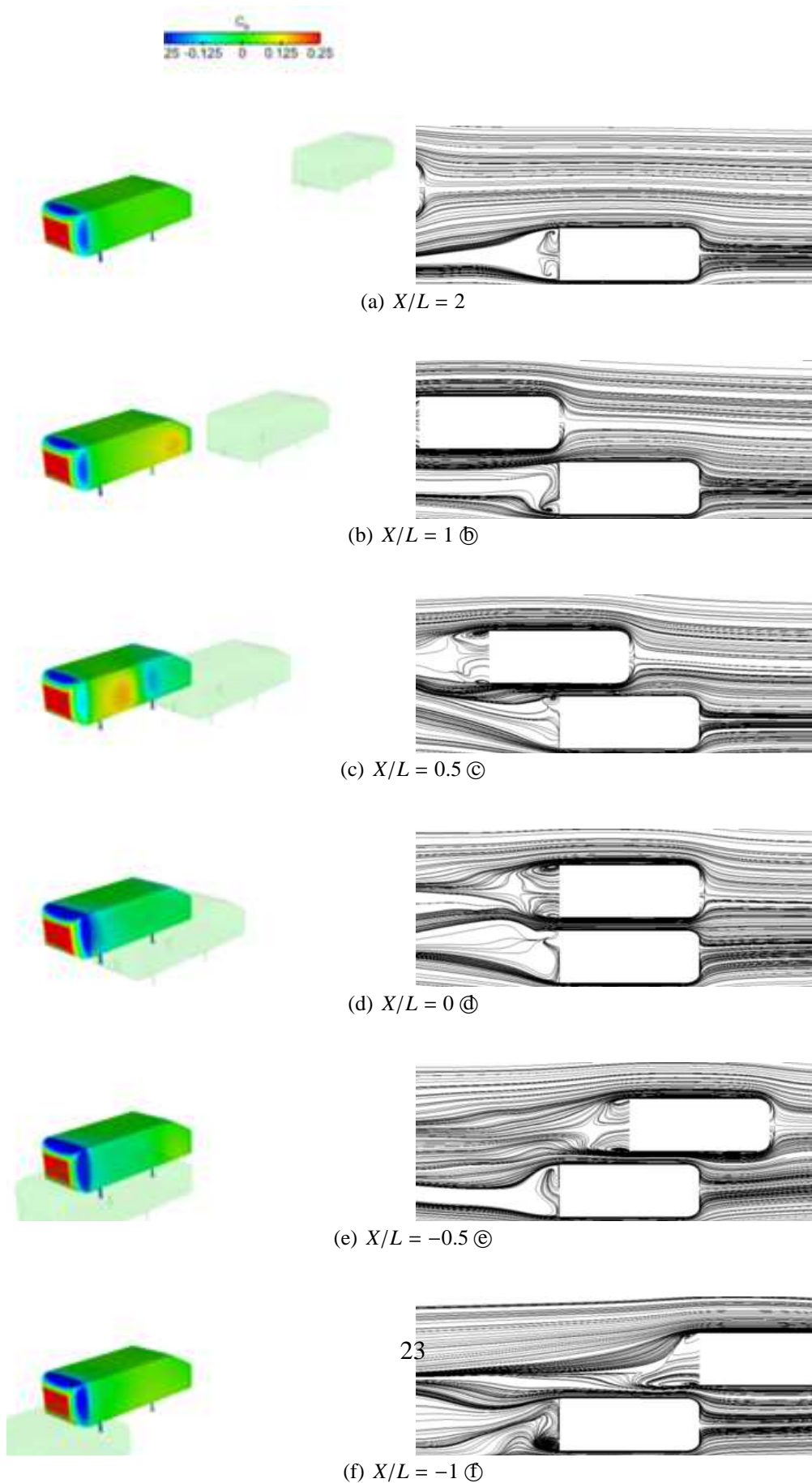


Figure 12: Left: Surface pressure coefficient on the overtaken vehicle. Right: Streamlines of the velocity field projected on the plane  $z = 0.1558 \text{ m}$ .

The evolution of the pressure coefficient,  $C_p = 2(p - p_\infty)/\rho V_\infty^2$  where  $p - p_\infty$  is the relative pressure, on the inner side of the overtaken vehicle can bring a first explanation. The pressure distributions are shown in the left hand column of figure 12 for the five moments corresponding to the vertical lines of figure 11 and for the position  $X = 2L$  which shows the steady state pressure, i.e. without the influence of the overtaking vehicle. The right hand column of figure 12 presents the instantaneous streamlines of the velocity field projected onto the plane  $z = 0.1558 \text{ m}$ , half of the total height of the vehicle, for the six previous positions.

#### 4.1.1. Flow between $X/L = 2$ and $X/L = 1$ (Ⓔ)

The drag force slightly increases before it experiences a sudden pulse. The high pressure in front of the overtaking body increases the pressure at the aft of the overtaken body yielding a drag reduction. After that, the negative pressure in the front side of the overtaking body reduces the pressure at the aft of the overtaken body. The pressure is reduced more and more because the narrowing of the space between both bodies involves an acceleration of the flow. This pressure decrease at the aft of the overtaken body explains the drag pulse at  $X/L = 1$  (Ⓔ) in figure 11.

The side force increases. As shown in figure 12(b) (left), after its action on the aft of the overtaken body, the high pressure in front of the overtaking body occurs on the inner side of the overtaken body. The result is to increase the side force.

The yawing moment decreases. The effect of the high pressure on the inner side



of the overtaken body is, at first, concentrated on the rear of the overtaken body, as shown in figure 12(b) (left). Then, only the rear of the overtaken body is repelled. Besides, the approaching of the overtaking body has an effect at the aft of the overtaken body. As can be seen in figure 12(b) (right), the flow separation from the overtaken body's rear end is influenced and the recirculating flow to the aft outer surface is shifted. This change of the flow yields a further anticlockwise moment.

#### 4.1.2. Flow between $X/L = 1$ (Ⓓ) and $X/L = 0.5$ (Ⓒ)

The drag force still increases because a low pressure still acts at the aft of the overtaken body.

The side force still increases slightly after Ⓓ before it decreases. The high pressure further increases the pressure on the inner side of the overtaken body involving the slight increase. When the front of the overtaking body overtakes the rear of the overtaken body, just after Ⓓ, the low pressure on the front side of the overtaken body reduces the pressure on the inner side of the overtaken body. This low pressure is added to a Venturi effect, which appears when bodies are close. This global low pressure effect is clearly visible in figure 12(c) (left). The reduction of the pressure induced explains the decrease of side force.

The reduction of the pressure on the inner side of the overtaken body is limited to the rear half, as shown in figure 12(c) (left), then the rear of the overtaken body is pulled into the path of the overtaking body. Therefore, the yawing moment

increases. Moreover, the high pressure is now acting on the front half of the overtaken body, as shown in 12(c) (left), repelling the front part of this body. As the front half of the overtaken body is repelled, the yawing moment further increases. The combined effects of the low pressure on the rear half of the overtaken body, and the high pressure on the front half of the overtaken body lead to the maximum value for the yawing moment in ©, figure 12(c) (left).

#### 4.1.3. Flow between $X/L = 0.5$ (©) and $X/L = 0$ (Ⓓ)

The drag force slightly increases before it decreases. The low pressure effect at the aft of the overtaken body reduces.

The side force still decreases and is now negative. The overtaking body passed the central region of the overtaken one, the low pressure effect is now predominating, as shown in figure 12(d) (left), and the overtaken body is further pulled towards the overtaking body. The effect of the low pressure on the inner side of the overtaken body is maximum when vehicles are side by side, at the position  $X/L = 0$  (Ⓓ). Therefore, the side force reaches its minimum value at this position.

The yawing moment decreases. After ©, the low-pressure effect also acts on the front half of the overtaken body, as shown in figure 12(d) (left), which means that the nose of the overtaken body is pulled into the path of the overtaking one.

#### 4.1.4. Flow between $X/L = 0$ (Ⓓ) and $X/L = -0.5$ (©)

The drag force still decreases and the value of the coefficient is lower than the steady value. The front of the overtaking body overtakes the front of the overtaken

body and the low pressure of the front side of the overtaking body decreases the pressure at the fore of the overtaken body. Therefore, the drag decreases.

The side force increases. The low pressure effect, on the inner side of the overtaken body, reduces. Both vehicles begin to repel each other.

The yawing moment slightly increases, after ④, before it decreases again. The yawing moment increases slightly because there is an interaction between the flow separations occurring at the aft edges of both bodies, figure 12(c) (right). This increase is not found in the experimental data for  $k = 0.248$ , see figure 6. However, it is visible for lower relative velocity  $k = 0.141$ , as shown in figure 7(b). After that, the low pressure effect is now acting almost on the front half of the overtaken body, then the front half of this body is pulled into the path of the overtaking body and the yawing moment decreases.

#### 4.1.5. Flow between $X/L = -0.5$ (③) and $X/L = -1$ (④)

The drag force remains constant to approximately  $X/L = 0.8$  before it increases. All the effects produced by the overtaking vehicle diminish and the drag coefficient returns to its steady value.

The side force still increases. Indeed, the low pressure further decreases.

The yawing moment experiences a slight decrease before it increases again.

#### 4.1.6. Flow between $X/L = -1$ (④) and $X/L = -2$

The drag force increase until its steady value.

The side force and the yawing moment experience a slight increase before they return to zero. As seen, in figure 13, a positive pressure part, from the rear of the overtaking body propagates towards the overtaken one. The inner sharp edge at the aft of the overtaking body produces a flow separation which repels the overtaken body, as shown in figure 12(f) (right). Furthermore, the flow at the aft of the overtaken body, figure 12(f) (right), is similar to the flow at the position  $X/L=1$ , figure 12(b) (right). The inner flow separation is disrupted by the flow at the aft of the overtaking body and the outer recirculating flow is shifted. This disruption yields to further increase the yawing moment.

The numerical peak of side force after ①, does not exist in the experimental data, see figure 6. It can be noted that this peak appears on experimental results for lower  $k$  in [6] which are, unfortunately, difficult to consider numerically because of large computational times. This result is inconsistent with the numerical results of Corin et al [12] for which rounded edges models are used. However, it is consistent with the numerical results of Clarke and Filippone [11] for which sharp edges are used. Moreover, Gilliéron [13] obtained the same kind of behavior with his simulations of 3D slanted Ahmed bodies. This peak is induced by the flow separation occurring at the inner sharp edge at the aft of the overtaking body. At this point it is not clear if this difference between present prediction and experimental data is related to poor modeling of URANS or to experimental data.

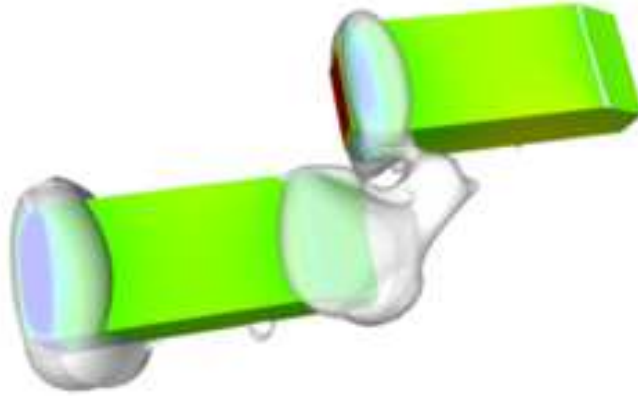


Figure 13: Isosurface of pressure,  $p=20$  Pa. At the position  $X/L=-1$ .

#### 4.1.7. At $X/L = -2$

All the coefficients are returned to their steady values, the overtaking body does not have effect on the overtaken body any more.

## 5. Conclusions

A three-dimensional numerical methodology, with a deforming/sliding mesh method and the  $\zeta - f$  turbulence modelling, was successfully employed to simulate the dynamic passing process between two vehicles. Studies, performed in this work, have highlighted the capacities of the numerical method to well reproduce the effect of the relative velocity and of the lateral spacing on the aerodynamic forces and moments. A complete analysis has enabled to explain all the effects acting on the vehicles.

For the overtaken vehicle, it was shown that an increase of transversal spacing involves a decrease of aerodynamic coefficients amplitudes. Moreover, amplitudes of coefficients evolve linearly with the logarithm of the lateral spacing, which confirms the experimental results. Similarly, the aerodynamic coefficients peaks decrease when the relative velocity increases. This conclusion is obviously dependent of the choice of the steady velocity.

The future work will extend the present study to overtaking between vehicles with different sizes like a truck and a car. Furthermore, the overtaking in gusty winds will be studied because of safety implications of combination of gusty winds and vehicle overtaking.

## Acknowledgments

This work is supported financially by the Area of Advance Transport at Chalmers. Software licenses were provided by AVL List GMBH. Computations were performed at SNIC (Swedish National Infrastructure for Computing) at the Center for Scientific Computing at Chalmers (C3SE) and National Supercomputer Center (NSC) at Linköping University.

## References

- [1] R. K. Heffrey, Aerodynamics of passenger vehicles in close proximity to trucks and buses, SAE paper (1973) 901 – 914.
- [2] J. P. Howell, The influence of the proximity of large vehicle on the aerodynamic characteristics of a typical car. advances in road vehicle aerodynamics, bhra, fluid engineering (1973) 207 – 221.
- [3] T. Legouis, P. Bourassa, V. D. Nguyen, Influence d'un poids lourd équipé ou non de dispositifs aérodynamiques sur une automobile en manœuvre de dépassement, Journal of Wind Engineering and Industrial Aerodynamics 9 (1984) 381 – 387.
- [4] D. P. Telionis, C. J. Fahrner, G. S. Jones, An experimental study of highway aerodynamic interferences, Journal of Wind Engineering and Industrial Aerodynamics 17 (1984) 267 – 293.

- [5] S. Yamamoto, K. Yanagimoto, H. Fukuda, H. China, K. Nakagawa, Aerodynamic influence of a passing vehicle on the stability of the other vehicles, JSAE Review 18 (1997) 39 – 44.
- [6] C. Noger, E. Széchenyi, Experimental study of the transient aerodynamic phenomena generated by vehicle overtaking, 8th International Conference on Flow-Induced Vibrations (FIV), Ecole Polytechnique, Paris (France) (2004).
- [7] C. Noger, C. Regardin, E. Széchenyi, Investigation of the transient aerodynamic phenomena associated with passing manoeuvres, Journal of Fluids and Structures 21 (2005) 231 – 241.
- [8] S. R. Ahmed, G. Ramm, G. Faltin, Some salient features of the time averaged ground vehicle wake (1984). SAE Paper 840300.
- [9] C. Noger, E. V. Grevenynghe, On the transient aerodynamic forces induced on heavy and light vehicles in overtaking processes, Int. J. Aerodynamics 1 (2011) 373 – 383.
- [10] P. Gilliéron, C. Noger, Contribution of the analysis of transient aerodynamic effects acting on vehicles, SAE paper no. 2001-01-1311 (2004).
- [11] J. Clarke, A. Filippone, Unsteady computational analysis of vehicle passing, Journal of Fluid Engineering 129 (2007) 359 – 367.



- [12] R. J. Corin, L. He, R. G. Dominy, A CFD investigation into the transient aerodynamic forces on overtaking road vehicle models, *Journal of Wind Engineering and Industrial Aerodynamics* 96 (2008) 1390 – 1411.
- [13] P. Gilliéron, Detailed analysis of the overtaking process, *Journal of Mechanical Engineering* 53 (2003).
- [14] K. Hanjalić, M. Popovac, M. Hadžiabdić, A robust near-wall elliptic-relaxation eddy-viscosity turbulence model for CFD, *International Journal of Heat and Fluid Flow* 25 (2004) 1047–1051.
- [15] C. G. Speziale, S. Sarkar, T. B. Gatski, Modelling the pressure-strain correlation of turbulence: an invariant dynamical systems approach, *Journal of Fluid Mechanics* 227 (1991) 245–272.
- [16] P. A. Durbin, Near-wall turbulence modeling without damping functions, *Theoretical and Computational Fluid Dynamics* 3 (1991) 1–13.
- [17] S. Krajnović, E. Bjerklund, B. Basara, Simulations of the flow around high-speed train meeting each other at the exit of a tunnel, *21st International Symposium of Dynamics of Vehicles on roads and Tracks* (2009).
- [18] S. Krajnović, A. Bengtsson, B. Basara, Large eddy simulation investigation of the hysteresis effects in the flow around an oscillating ground vehicle, *ASME Journal of Fluids Engineering* 133 (2011).